

## Optimization design about end plates of ship rudder based on hydrodynamic numerical simulations



Lixun Hou<sup>1,\*</sup>, Ye Han<sup>2</sup>, Ruizhong Wang<sup>1</sup>

<sup>1</sup> College of Ocean Science and Engineering, Shandong University of Science and Technology, Qingdao 266590, China

<sup>2</sup> Tianjin Haoye Technology Co., Ltd, Tianjin 300400, China

### ARTICLE INFO

Keywords:

Rudder

End plate

Hydrodynamic performance

Optimization

### ABSTRACT

To further improve the hydrodynamic performance of ship rudder systems, the addition of end plates at the upper and lower ends of the rudder blade can effectively suppress transverse flow. This study investigates the influence of such end plates on the hydrodynamic characteristics of a ship rudder, exploring the optimal configuration through comprehensive numerical simulations. Hydrodynamic performance comparisons are conducted between a rudder equipped with end plates and a conventional rudder across various rudder angles. The results indicate that end plates significantly enhance both rudder lift and the lift-to-drag ratio compared to the conventional design, with the magnitude of improvement increasing at larger rudder angles. The beneficial effect of end plates on rudder efficiency becomes particularly pronounced during large-angle manoeuvres. Through systematic optimization based on hydrodynamic simulations, the optimal geometric parameters of the end plates are identified. For the rudder studied in this work, the optimal width, chordwise length before the leading edge and chordwise length after the trailing edge of the end plate are found to be 0.16, 0.03 and 0.05 times the chord length of the rudder, respectively. This research provides a valuable technical foundation for improving the design of ship manoeuvring systems, contributing to more efficient and responsive marine navigation solutions.

### 1. Introduction

Enhancing the manoeuvrability of marine vessel while striving for greater energy efficiency and reduced emissions has become a central focus for maritime professionals. As a critical control element in ship navigation, rudder hydrodynamic performance plays a key role in ensuring operational safety and minimizing fuel consumption during voyages. Consequently, exploring the functional principles and design methodologies of ship rudders is of significant importance to the advancement of marine engineering practices.

To enhance the operational efficiency of ship rudders, researchers worldwide have extensively investigated their design and functionality. As traditional streamlined rudders offer limited potential for further energy efficiency improvements, a variety of innovative rudder configurations have been developed and

\* Corresponding author.

E-mail address: [07093129@163.com](mailto:07093129@163.com)

systematically studied. These include twisted rudders [1], rudder-attached thrust fins [2], fishtail rudders, flap rudders [3, 4], collaborative spoiled rudders [5, 6], gate rudders [7, 8], magnus rudders [9, 10], among others. These designs aim to enhance propulsion performance and, therefore, either improve ship speed or significantly increase manoeuvrability. However, most ship rudders are usually small-aspect-ratio, symmetrical, wing-shaped structures that are prone to pronounced endwise transverse flow during operation. This transverse flow increases the rudder's induced drag, reduces the effective chordwise velocity circulation, and ultimately degrades the rudder's hydrodynamic efficiency and effectiveness [11].

One effective method to suppress this transverse flow is by adding end plates to the top and bottom of the rudder. End plate can enhance rudder lift, increase effectiveness, and improve overall ship manoeuvrability. Their structure simplicity and minimal impact on steering gear power requirements make them particularly suitable for retrofitting existing vessels [12]. To improve the manoeuvrability of a Very Large Crude Carrier (VLCC) with limited engine output, Zaky et al. [13] designed a high-lift rudder incorporating end plates and a fishtail section to enhance rudder force while minimizing additional resistance. The results showed that the high-lift rudder increased effective rudder force by approximately 10% compared to a conventional mariner rudder. While end plates have been shown to significantly improve rudder performance, most existing studies have focused on the overall performance benefits rather than conducting detailed investigations into their hydrodynamic characteristics. Furthermore, systematic optimization of end plate design remains largely unexplored.

To further improve the performance of rudders equipped with end plates, this investigation focuses on elucidating the underlying hydrodynamic mechanisms and systematically optimizing end plate configurations using numerical simulation techniques. In recent years, Computational Fluid Dynamics (CFD) method has been extensively applied in marine engineering applications for hydrodynamic analysis [14-17]. The CFD method is particularly effective in analyzing structures with complex geometries and capturing detailed flow field characteristics under complex working conditions by providing detailed flow field data, such as pressure and velocity distributions. Regarding naval rudder systems, Tian [18] implemented CFD simulations using FLUENT software to evaluate the hydrodynamic performance of a flap rudder design under open-water conditions, and apply these numerical insights to vessel turning radius calculations. Moreover, Liu et al. [19] employed Reynolds-Averaged Navier-Stokes (RANS) formulations to assess the hydrodynamic characteristics of diverse rudder profiles, quantitatively establishing correlations between profile geometry and vessel manoeuvrability. In addition, Shin et al. [20] executed comprehensive CFD analyses of wavy twisted rudders in a propeller wake, validating their findings with experimental datasets and demonstrating benefits such as delayed flow separation and enhanced lift-to-drag ratios. Furthermore, Yang et al. [21] explored the effects of skeg-flap clearance on flap rudder hydrodynamics using RANS-based simulations, offering insights into force generation and vortex evolution, with strong alignment with experimental measurements. Added to that, Sukas et al. [22] employed both system-based and direct CFD approaches to evaluate twisted rudder performance during ship manoeuvres, revealing significant flow asymmetry and nonlinear hydrodynamic responses. Moreover, Park et al. [23] proposed an innovative twisted rudder design methodology, validated through RANS simulations and experimental comparisons. Furthermore, Tong et al. [24] utilized Large Eddy Simulation (LES) to analyze the effects of asymmetric upstream rudder configurations on propeller thrust dynamics, focusing on transient flow characteristics and unsteady force generation at various rudder angles. In addition, Zhang et al. [25] examined vibration characteristics of rudders immersed in propeller wakes using Detached Eddy Simulation (DES), coupling fluid-structure interaction simulations with finite volume structural deformation solutions. Finally, Hou et al. [5] proposed a novel collaborative spoiled rudder configuration, integrating hydrodynamic advantages of conventional designs with DES simulations. This approach demonstrated significant performance enhancements over traditional rudder systems. Subsequent two-dimensional (2D) parametric studies [6] optimized angular configurations for both the main rudder and spoiler control surfaces based on detailed hydrodynamic evaluations.

The numerical simulations conducted in this study for the hydrodynamic analysis and optimization of the End Plate Rudder (EPR) employ the DES method. This approach is first validated through an analysis of the hydrodynamic performance of a conventional rectangle rudder. Then, both the Conventional Rudder (CR)

and the EPR with a specific configuration are investigated across various rudder angles to assess the overall impact of end plates on rudder hydrodynamic performance. Building on these results, the EPR with end plates of varying sizes are studied to determine the impact of end plate dimensions on the hydrodynamic performance, leading to the identification of the optimal geometric parameters. The findings of this study aim to provide technical guidance for the design work of the EPR.

## 2. Methods and hydrodynamic expressions

In this study, a viscous flow CFD framework is utilized to conduct numerical simulations of a ship rudder's hydrodynamic performance. The flow field is simulated via the DES method whereas the SST  $k-\omega$  model is used to close RANS equations. The SST  $k-\omega$  DES model combines the features of SST  $k-\omega$  RANS in the boundary layers with the LES model in other regions. Concerning the DES model, the momentum equations for the RANS averaged velocity  $\bar{v}$  and LES filtered velocity  $\tilde{v}$  are defined in the tensor form with Cartesian coordinates expressed as follows:

$$\frac{\partial}{\partial t}(\rho\bar{v}) + \nabla \cdot (\rho\bar{v} \otimes \bar{v}) = -\nabla \cdot \bar{p}I + \nabla \cdot (T + T_i^{RANS}) + f_b \quad (1)$$

$$\frac{\partial}{\partial t}(\rho\tilde{v}) + \nabla \cdot (\rho\tilde{v} \otimes \tilde{v}) = -\nabla \cdot \tilde{p}I + \nabla \cdot (T + T_i^{LES}) + f_b \quad (2)$$

where  $\rho$ ,  $I$  and  $T$  represent the fluid density, identity tensor, and viscous stress tensor, respectively. Moreover,  $f_b$  is the resultant body force,  $\bar{p}$  denotes the fluid pressure in RANS simulation, and  $\tilde{p}$  is that in the LES simulation. Finally,  $T_i^{RANS}$  designates the Reynolds-stress tensor for the RANS model and  $T_i^{LES}$  represents that for the LES model.

The Reynolds-stress tensor  $T_i^{RANS}$  is a function of the time- and length-scale in a RANS model, expressed as follows:

$$T_i^{RANS} = f(\nabla \cdot \bar{v}, k, \varepsilon) \quad (3)$$

For LES, the Reynolds-stress tensor  $T_i^{LES}$  is described by a velocity defined by filter width or length scale and expressed as follows:

$$T_i^{LES} = f(\nabla \cdot \tilde{v}, \Delta) \quad (4)$$

where  $\Delta$  is the local measure of the grid size.

Moreover, the variables in the DES momentum equation depend on the time- and length-scale of the RANS solution or on functions of the filter width or length scale in the LES model. The transition from RANS to LES is accomplished by a specific length scale  $\hat{l}$ , expressed as follows:

$$\hat{l} = \min(l_{k-\omega}, C_{DES}\Delta) \quad (5)$$

where  $l_{k-\omega}$  is the length scale in the RANS solution,  $C_{DES}$  represents a model coefficient (typically set to 0.65 for homogeneous turbulence), and  $\Delta = \max(\Delta_x, \Delta_y, \Delta_z)$  denotes the maximum cell size, where  $\Delta_x$ ,  $\Delta_y$ , and  $\Delta_z$  are cell characteristic mesh spacing indicators in all spatial directions. When the cell length  $C_{DES}\Delta$  is smaller than the RANS length scale  $l_{k-\omega}$ , the LES simulation (refer to Eq. (2)) is triggered; otherwise, the RANS simulation (Eq. (1)) is used. A more complete and detailed description of the DES method is available in a previously published work by Shur et al. [26].

The pressure and velocity coupling is solved using the SIMPLE method. A second-order convection scheme is adopted for the momentum equations. Transport equations of the SST  $k-\omega$  turbulence model are computed using second-order upwind and central difference schemes. A second-order implicit scheme is used for temporal discretization and five inner iterations per time step are used. The all- $y^+$  wall treatment is utilized to predict the flow and turbulence parameters across the wall boundary layer. Unsteady simulations are

performed, where the Courant-Friedrichs-Lewy (CFL) condition is applied to balance temporal and spatial scales according to the minimum grid resolution.

To accurately represent the hydrodynamic parameters (lift and drag) of the ship rudder, a reference coordinate system O-XYZ is established, as illustrated in Fig. 1. The origin O of this reference coordinate system is located at the center point of the rudder stock. The X-axis points in the direction of the flow, the Y-axis points starboard, whereas the Z-axis is determined by the right-hand rule. The angle between the chord line of the rudder and the X-axis is defined as the rudder angle  $\alpha$ . This study primarily investigates the global lift  $L$  (force component in the Y-axis direction) and drag  $D$  (force component in the X-axis direction). Relevant hydrodynamic parameters are expressed dimensionless as follows:

$$C_L = \frac{L}{0.5\rho V_0^2 A_R} \quad (6)$$

$$C_D = \frac{D}{0.5\rho V_0^2 A_R} \quad (7)$$

where  $\rho$  is the water density,  $V_0$  represents the inflow velocity,  $A_R$  denotes the rudder area, and  $C$  designates the chord length.

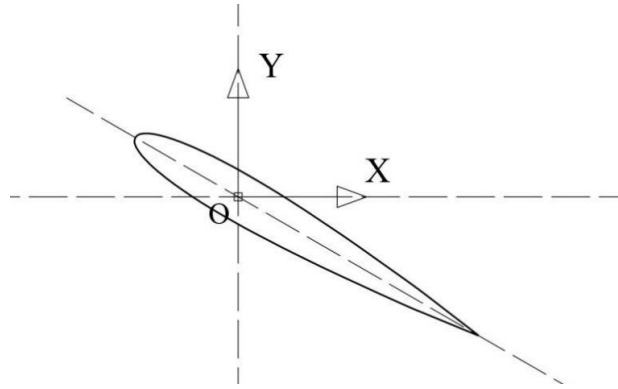


**Fig. 1** Rudder coordinate system

### 3. Research subject

Considering that NACA0020 profile is often used for marine rudders, whose type rudder has complete experimental data, this research undertakes numerical simulations on a ship rudder featuring NACA0020 profile. The rudder blade has a chord length of  $C = 240$  mm and an aspect ratio of  $\lambda = 1$ . A modified version of the rudder with end plates is developed by attaching two end plates to the upper and lower ends of the rudder blade, as depicted in Fig. 2. The end plate has a rectangular structure with a thickness of  $0.005C$ . The key parameters of the end plates are illustrated and defined in Fig. 3, where parameter  $c$  indicates the chordwise length before the leading edge of the rudder blade, whereas  $d$  represents the chordwise length after the trailing edge. In addition,  $b$  stands for the half-width, and  $r$  denotes the radius of the rounded corners applied to all four corners of the end plate.

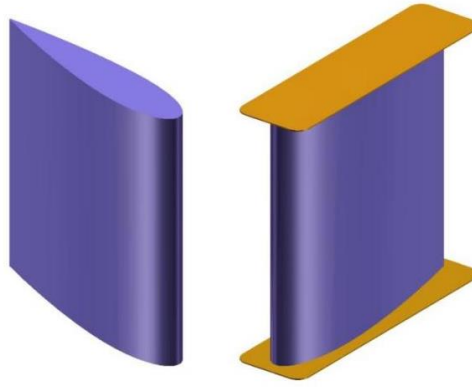


**Fig. 2** Rudders without end plates (left) and with end plates (right)

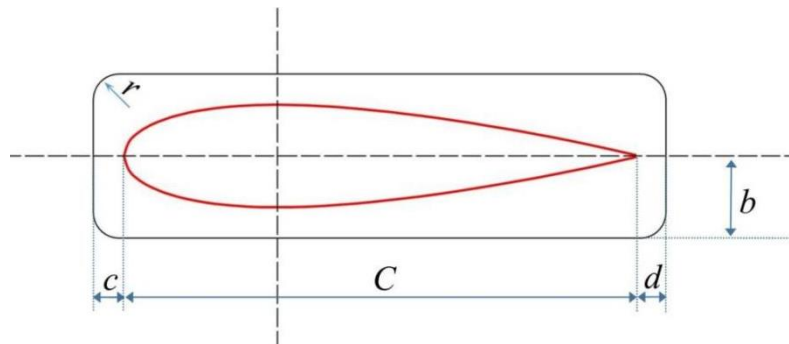


**Fig. 3** Parameter terminologies of end plate

This study aims to investigate the impact of end plates on the hydrodynamic performance of a rudder. Numerical simulations are conducted to optimize the end plate key parameters. Parametric calculations are carried out to determine the optimal values for the end plate chordwise lengths ( $c$  and  $d$ ) and half width ( $b$ ). The radius ( $r$ ) of the rounded corners of the end plate is kept constant and set at  $0.05C$  for all scenarios. Table 1 shows the values of the different parameters considered in this study. Different configurations of the end plate are generated when changing its chordwise lengths and the width.

**Table 1** Parameter values of end plate for optimization design

$b$	$c$	$d$
$0.13C$	$0.02C$	$0.02C$
$0.14C$	$0.03C$	$0.03C$
$0.15C$	$0.04C$	$0.04C$
$0.16C$	$0.05C$	$0.05C$
$0.17C$	$0.06C$	$0.06C$
$0.18C$	$0.07C$	$0.07C$
	$0.08C$	$0.08C$

#### 4. Computational domain and grid generation

The computational domain is defined for numerical simulations about rudders. Fig. 4 depicts the computational domain established in the shape of a cylinder, having a radius of  $5C$ . The inlet and outlet are located at distances of  $5C$  and  $10C$  from the rudder stock, respectively. The inlet boundary and side surfaces are set as velocity inlets with an inlet velocity of  $2.904$  m/s, whereas the outlet boundary is set as a pressure outlet. The rudder surface is developed as a non-slip wall.

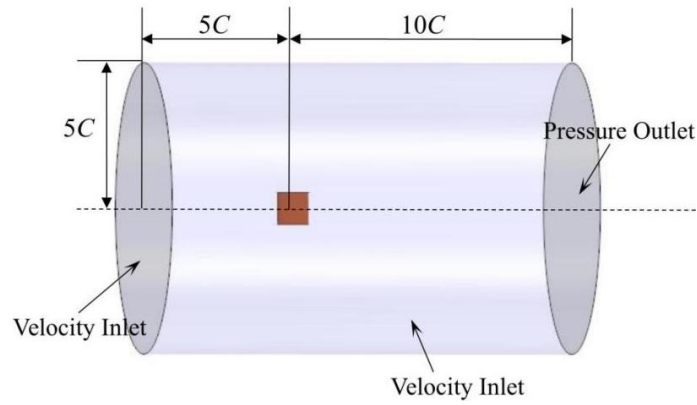


**Fig. 4** Domain for numerical simulations

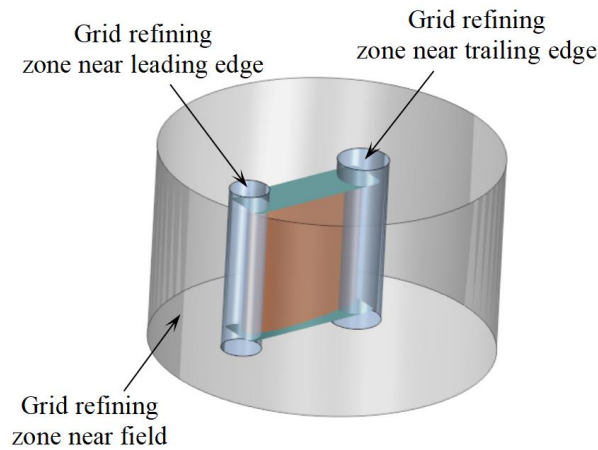


**Fig. 5** Grid refining zones around rudder

In this study, the computational grid for simulations is generated using the integrated polyhedral meshing tool within STAR-CCM+, which is also used for the numerical simulations in this work. This approach leverages adaptive refinement techniques to optimize computational efficiency by strategically trimming grid elements in the flow domain, reducing cell count while preserving solution accuracy. To accurately resolve complex flow features, the local grid refinement is applied near the rudder surface and its leading/trailing edges, as illustrated in Fig. 5.

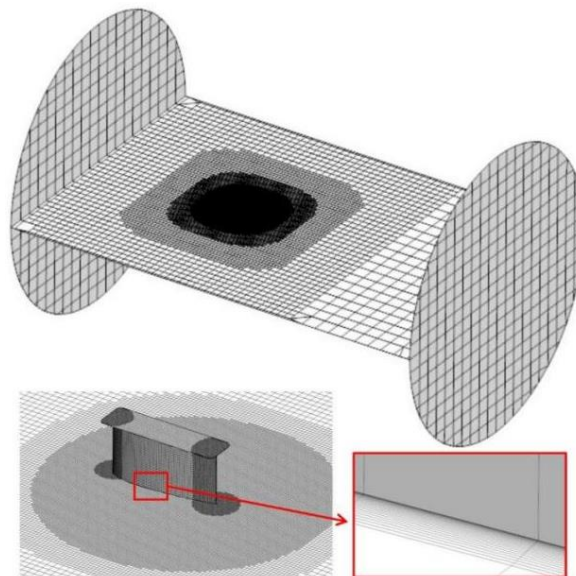


**Fig. 6** Grid generated for numerical simulations

Fig. 6 illustrates the entire computational domain grid and the local grid surrounding the rudder. To precisely simulate the boundary layer, prism layers are configured. A target  $y^+$  set to 0.5 is used to calculate the thickness of the first layer of the prism layers, satisfying the requirements of the SST  $k-\omega$  model. The growth rate of the boundary layer mesh is set at 1.1, having a total of 25 layers. This setup ensures that the overall thickness of the boundary layer is roughly equivalent to the mesh size in the refined region of the rudder's leading and trailing edges.

## 5. Grid convergence analysis

In numerical simulations, the grid partitioning strategy plays a crucial role in determining computational accuracy. In this study, a grid convergence analysis of the conventional rudder is performed to identify the most optimal grid partitioning strategy, and the reliability of the numerical approach is evaluated by comparing simulation results with experimental data. Seven grid configurations from G01 to G07 in ascending order of grid quantity are generated. The grid configurations from G02 to G07 are generated from G01 by proportionally refining the grid spacing at a fixed ratio of 1.2. For G01, the grid size in the far field and its boundaries is  $0.7C$ , and the rudder surface grid size is  $0.02C$ . The grid size in the local refinement zone near the rudder surface is  $0.02C$ , and that in the local refinement zones near the rudder's leading/trailing edges is  $0.01C$ . The thickness of the first boundary layer cell is maintained constant and determined by  $y^+=0.5$ . The total grid numbers for different grid configurations are given in Table 2.

The hydrodynamic performance is computed at rudder angles of  $10^\circ$ ,  $20^\circ$ , and  $30^\circ$ . The lift ( $C_L$ ) and drag ( $C_D$ ) are selected as the primary performance indicators. The time step in each simulation is controlled using the Courant-Friedrichs-Lewy (CFL) number, with a maximum CFL number set to 1.0 and an average CFL number of 0.5. Fig. 7 displays the  $y^+$  distribution on the rudder surface at  $\alpha=30^\circ$ , confirming that the values of  $y^+$  meets the requirements of the turbulence model. The hydrodynamic forces of rudder using different grid numbers at various rudder angles are displayed in Fig.8. It can be seen that the impact of the grid number on the hydrodynamic forces gets more obvious as the rudder angle increases. This indicates that, under large rudder angles, the numerical simulation results are more sensitive to mesh density. Overall, the lifts and drags at various rudder angles decrease gradually with the increase of grid number. When the grid number exceeds  $3.61 \times 10^6$  (G04), the calculation results tend to stabilize, and the number of meshes has little impact on the calculation results.

The hydrodynamic forces obtained using G04 are compared to the experimental data sourced from Feng's research [27], as given in Table 3. The lift calculated using the G04 shows only a small discrepancy compared to the experimental data, the drag exhibits a larger deviation. Nevertheless, the overall agreement between the numerical simulation results and the experimental data is satisfactory, validating the use of this grid configuration for subsequent simulations.

**Table 2** Grid numbers for different grid configurations

G01	G02	G03	G04	G05	G06	G07
$0.97 \times 10^6$	$1.50 \times 10^6$	$2.33 \times 10^6$	$3.61 \times 10^6$	$6.02 \times 10^6$	$9.88 \times 10^6$	$16.11 \times 10^6$

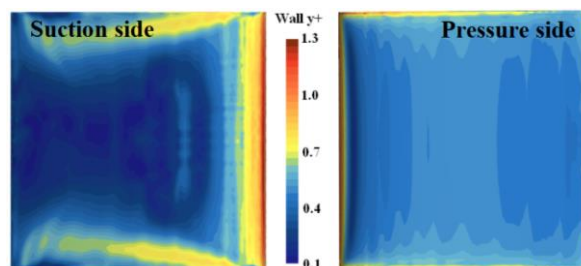


**Fig. 7** Wall  $y^+$  distribution on rudder surface at  $\alpha=30^\circ$

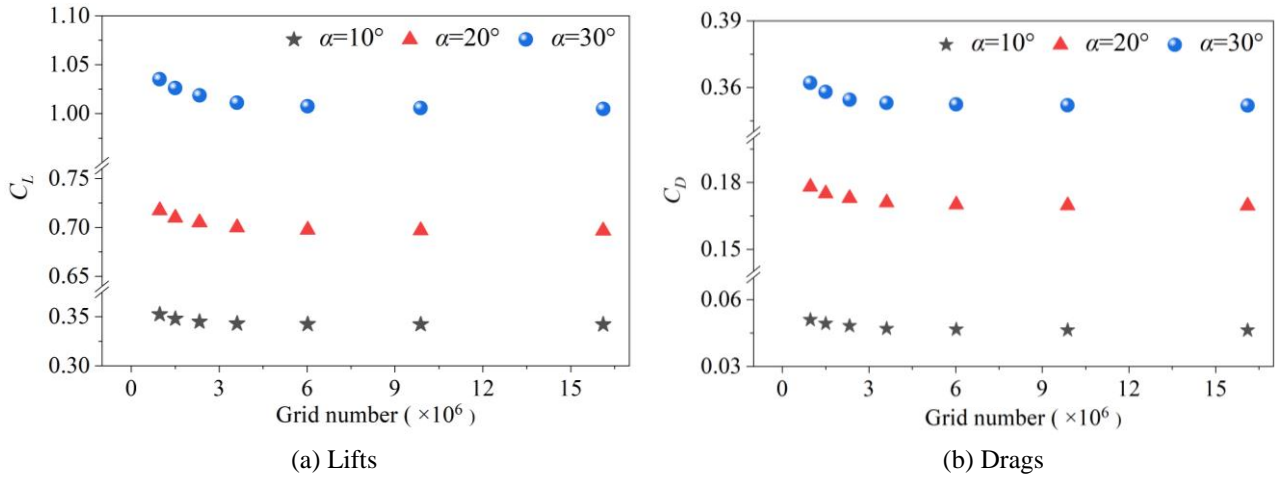


**Fig. 8** Hydrodynamic forces of rudder using different grid numbers at various rudder angles

**Table 3** Results of grid independence analysis and validation

$\alpha$	G04	Exp.	G04 error
$10^\circ$	0.343	0.335	2.68%
	0.047	0.044	7.11%
$20^\circ$	0.7	0.673	4.01%
	0.171	0.156	9.61%
$30^\circ$	1.011	1.02	0.88%
	0.353	0.349	1.15%

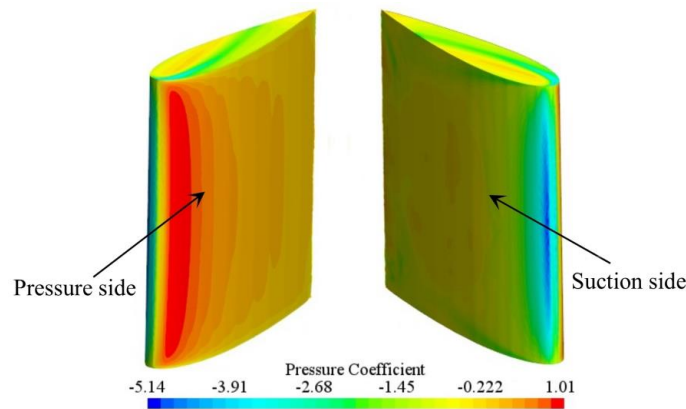


**Fig. 9** Pressure distribution on rudder surface at  $\alpha=30^\circ$

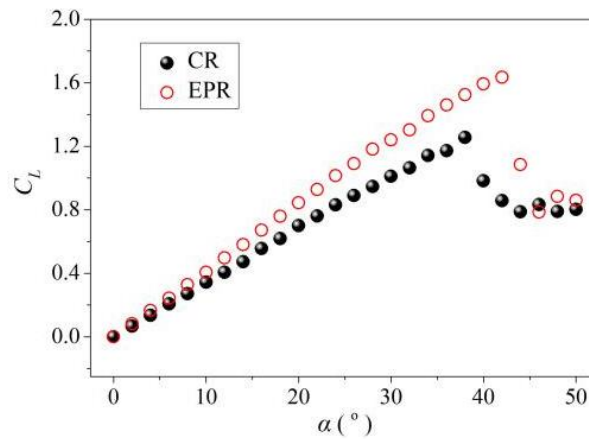
Fig. 9 presents the pressure distribution on the surface of the rudder blade obtained from the numerical simulation using the G04 grid at  $\alpha=30^\circ$ . It is evident that the pressure on the pressure side is significantly higher than that on the suction side. A pronounced high-pressure region is observed near the leading edge on the pressure side, while a corresponding low-pressure region appears near the leading edge on the suction side. Due to the end effect, this phenomenon gradually weakens towards both ends along the spanwise direction. The endwise transverse flow reduces the rudder efficiency to some extent.

## 6. Results for specific end plate configuration

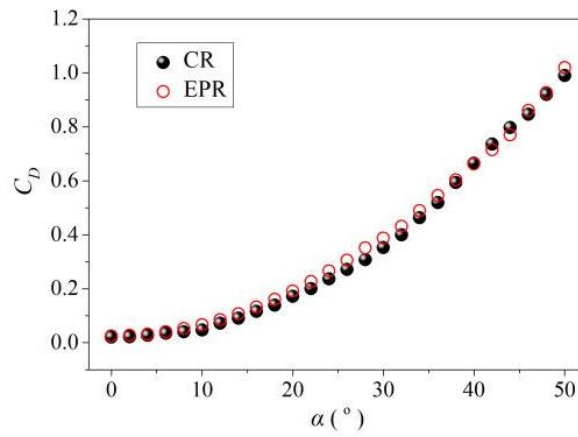
To reveal the overall impact of end plates on the hydrodynamic performance of the rudder, the Conventional Rudder (CR) and End Plate Rudder (EPR), with a specific configuration of  $c = d = 0.05C$  and  $b = 0.15C$ , are analyzed at rudder angles ranging from  $0^\circ$  to  $50^\circ$ , with an interval of  $2^\circ$ .

Fig. 10 displays the hydrodynamic forces of CR and EPR across a range of rudder angles. As the rudder angle increases, the lift generated by both CR and EPR initially increases, then declines. The CR experiences

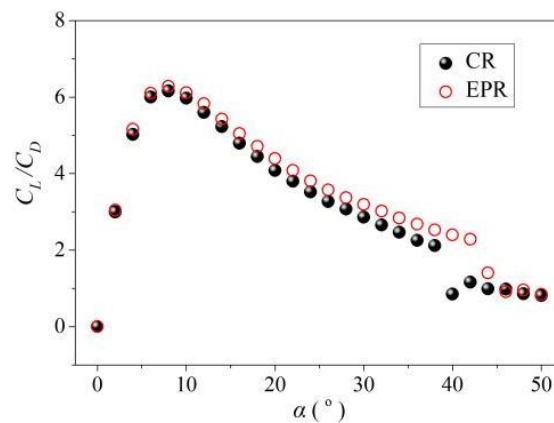
stall at approximately  $38^\circ$ , while the EPR stalls near  $42^\circ$ , indicating that the addition of end plates significantly delays stall in the EPR configuration. More importantly, EPR significantly increases the lift compared to CR, while the improvement in lift becomes more pronounced as the rudder angle increases before stall. The maximum lift of the EPR is approximately 30% higher than that of CR, representing its superior effectiveness. The drags characteristics of both EPR and CR exhibit similar changing trends with respect to rudder angle. The drag of EPR is much closer to that of CR at small ( $\alpha < 10^\circ$ ) or large ( $\alpha > 38^\circ$ ) rudder angles, whereas it is slightly higher than that of CR at rudder angles between  $10^\circ$  and  $38^\circ$ . The lift-to-drag ratio shows that both EPR and CR exhibit an increasing trend followed by a decreasing trend as the rudder angle increases with the optimal efficiency point for both types occurring at rudder angle of about  $8^\circ$ . Across different rudder angles, the efficiency of the EPR is always higher than that of the CR. This phenomenon becomes more pronounced as the rudder angle increases before stall.



(a) Lifts



(b) Drags



(c) Lift to drag ratios

**Fig. 10** Hydrodynamic forces of CR and EPR at different rudder angles

To further reveal the influence of end plates on the rudder's flow field characteristics, this study analyzes the vortical structures of EPR and CR at  $\alpha = 30^\circ$  (with  $Q = 200/s^2$ ), as shown in Fig. 11. The vortical structures are colored according to the local velocity magnitudes. For the CR, prominent rotating trailing vortices appear at the top and bottom ends of the rudder blade. These vortices gradually weaken from the midsection toward the blade ends, and a clear turbulent region is observed on the upper surface at the midsection. In contrast, the EPR exhibits significantly strengthened vortical structures due to the presence of end plates. A transverse trailing vortex is generated along the span of the rudder blade, extending uniformly at the top and bottom ends of the rudder blade, and interacting with the rotating vortices shedding from the ends. This leads to the formation of significant, fragmented vortical structures. The end plates effectively suppress transverse flow around the rudder blade and help inhibit turbulent separation on the upper surface of the rudder blade.

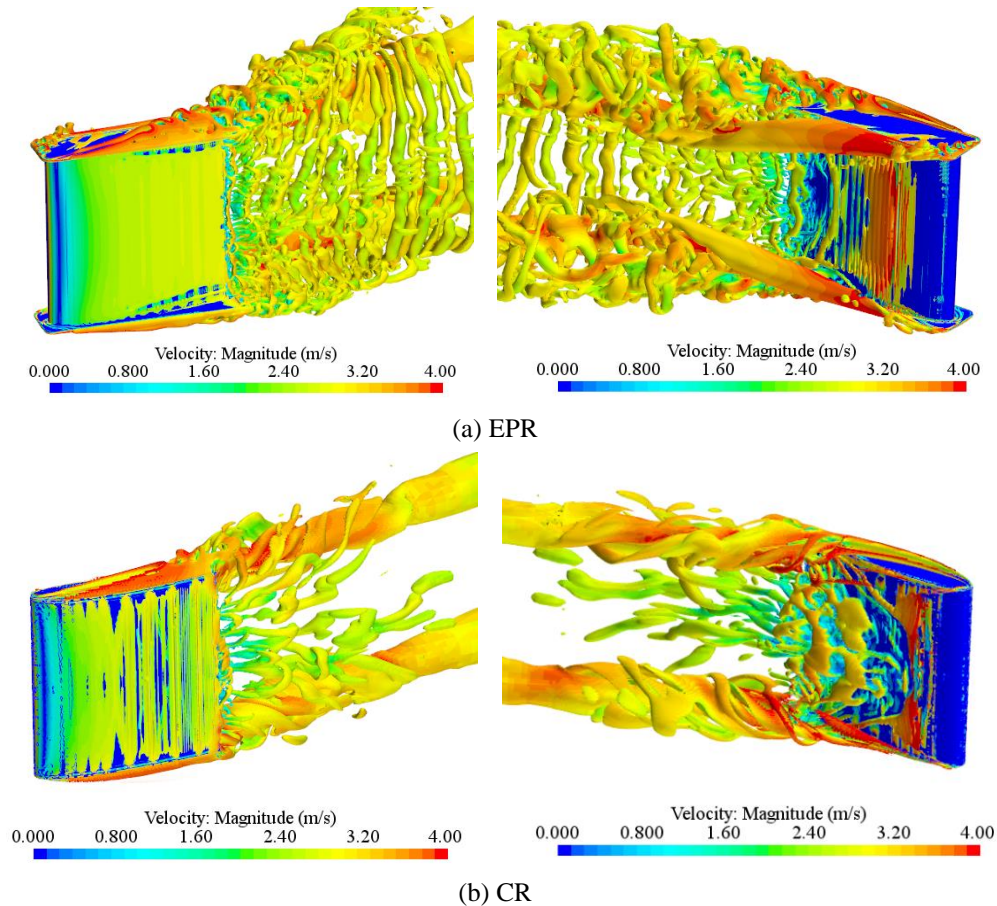


**Fig. 11** Vortical structures of EPR and CR at  $\alpha = 30^\circ$  ( $Q = 200/s^2$ )

To gain a deeper understanding of the effect of end plates on the transverse flow around the rudder blade, the pressure distribution along the rudder's height direction is analyzed. Specifically, the pressures values along two selected lines on the pressure sides of the lower and upper surfaces of the rudder blade are examined at  $X = 0.0C$  and  $X = 0.4C$ , representing  $0.3C$  and  $0.7C$  chordwise distances from the leading edge, respectively, as illustrated in Fig. 12.

Fig. 13 presents the pressure distributions along the selected pressure lines for both EPR and CR at rudder angles of  $10^\circ$ ,  $20^\circ$  and  $30^\circ$ , respectively. It is evident that the pressure on the lower surface is significantly higher than that on the upper surface, generating a pressure difference across various rudder angles. For the CR, notable pressure gradients appear near the top and bottom ends of the rudder blade due to transverse flow, with this effect becoming more obvious at  $X = 0.4C$ . In contrast, the EPR shows a substantial reduction in pressure gradients near the blade ends, especially at  $X = 0.0C$ , demonstrating the effectiveness of the end plates smoothing the pressure distribution along the rudder's height. The presence of pressure gradients forces the high-pressure fluid on the lower surface to flow around the rudder tips into the low-pressure region on the upper surface, forming end vortices, as shown in Fig. 11(b). The low-pressure region at the vortex core

increases the local pressure gradient. The interaction between the pressure gradient and vortices transforms the cross-flow from a passive response to an active transport mechanism, increasing boundary layer energy loss. This phenomenon is a key contributor to the rudder stall. Therefore, by reducing the pressure gradient at the rudder's ends, EPR exhibits higher hydrodynamic forces and delayed stall compared with CR.

The EPR exhibits lower pressure on the upper surface and higher pressure on the lower surface compared to CR. Therefore, the pressure difference between the lower and upper surfaces of the EPR is greater than that of the CR, and this difference becomes increasingly pronounced as the rudder angle increases before stall. This conclusion is mainly reflected in the rudder lift.

The pressure distributions of EPR and CR in the horizontal direction are also analyzed. Fig. 15 shows the corresponding pressure distribution on two horizontal cross-sections of the rudder blade at rudder angles of  $0^\circ$ ,  $10^\circ$ ,  $20^\circ$  and  $30^\circ$ , respectively. These cross-sections are located at the midsection ( $Z=0.0$  m) and the end section ( $Z=0.11$  m) of the rudder blade, as highlighted in Fig. 14. Given that rudder performance prior to stall is critical for ship maneuverability and navigation safety, this analysis focuses on pressure distributions under pre-stall conditions. Under the condition of non-steering, the pressure distribution on both sides of the rudder blade is completely symmetric, and no lift force is generated. The high-pressure region at the leading edge achieves slight expansion and at the trailing edge gets slight contraction due to the end plates. Thus, the resistance of rudder blade at  $\alpha=0^\circ$  yields minimal increase. Furthermore, the end plates themselves generate a certain amount of resistance, resulting in a moderate increase in the rudder's overall resistance. While steering, the low- and high-pressure regions gradually expand with the rudder angle. The location of the high-pressure region near the lower surface moves gradually towards the trailing edge as the rudder angle increases, whereas the low-pressure region moves forward.

The end plates change the pressure distribution near the rudder blade in the horizontal direction to some extent. For the midsection pressure, the high-pressure region near the EPR lower surface and the low-pressure region near the upper surface are higher than those of CR, and this difference becomes more pronounced with the increase of the rudder angle. When the rudder angle is small, the effect of the end plates on the midsection pressure can be neglected. For the pressure on the end section ( $Z=0.11$  m), the impact of the end plates becomes more pronounced. The pressure near the lower surface of EPR increases significantly; this phenomenon becomes more obvious as the rudder angle increases. However, beyond the region before the rudder section shoulder, the increase in pressure near the lower surface is accompanied by a corresponding increase near the upper surface from the section shoulder to the trailing edge, due to the influence of the end plates. As a result, the pressure on the upper surface at the ends of the EPR is higher than that of CR, consistent with the observations in Fig. 13. This behavior is mainly attributed to the end plates' ability to effectively suppress transverse flow at ends of the rudder blade, and the local stagnant flow is formed near the trailing edge. Therefore, the pressure near the upper surface at the rudder blade's ends increases from the section shoulder to the trailing edge. Conversely, before the section shoulder, the presence of the end plate causes a reduction in pressure on the upper surface.

Overall, combined with the results presented in Fig. 10, the beneficial impact of the end plates on the rudder's performance is more prominent at larger rudder angles before stall, as highlighted in Fig. 15.

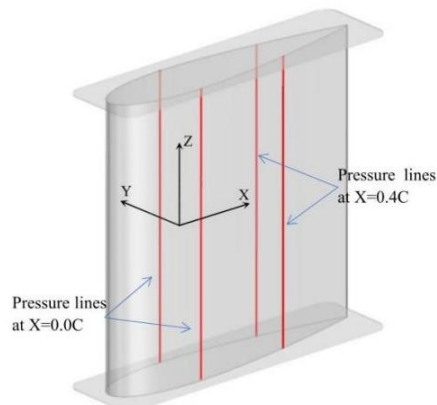


**Fig. 12** Pressure lines used for pressure analysis

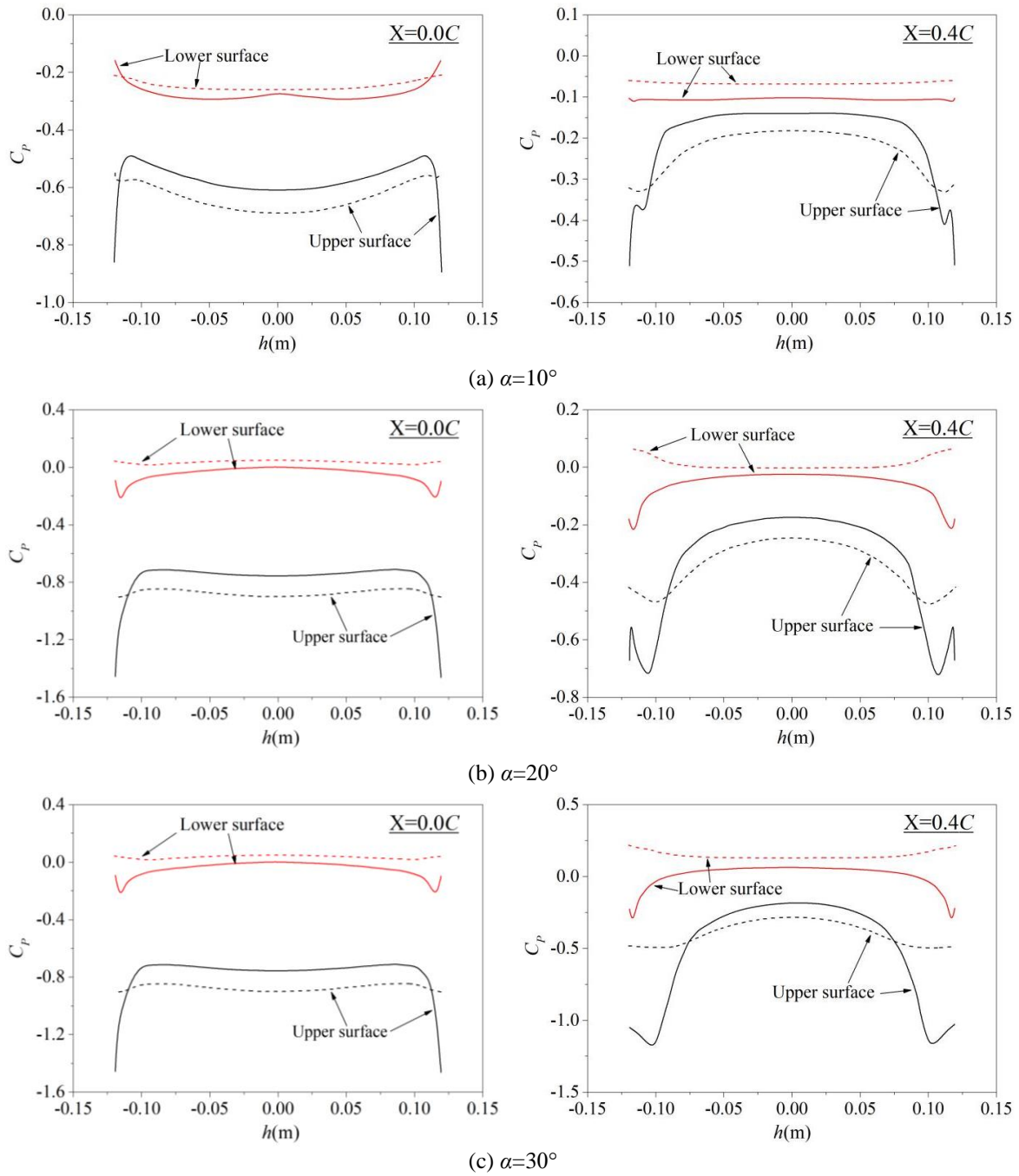


**Fig. 13** Pressure distributions along rudder's height direction (Dashed lines denote the results of the EPR and solid lines represent those of the CR)

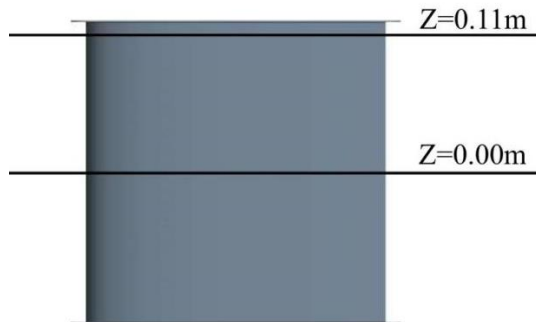


**Fig. 14** Horizontal cross-sections  $Z=0.0\text{m}$  and  $Z=0.11\text{m}$

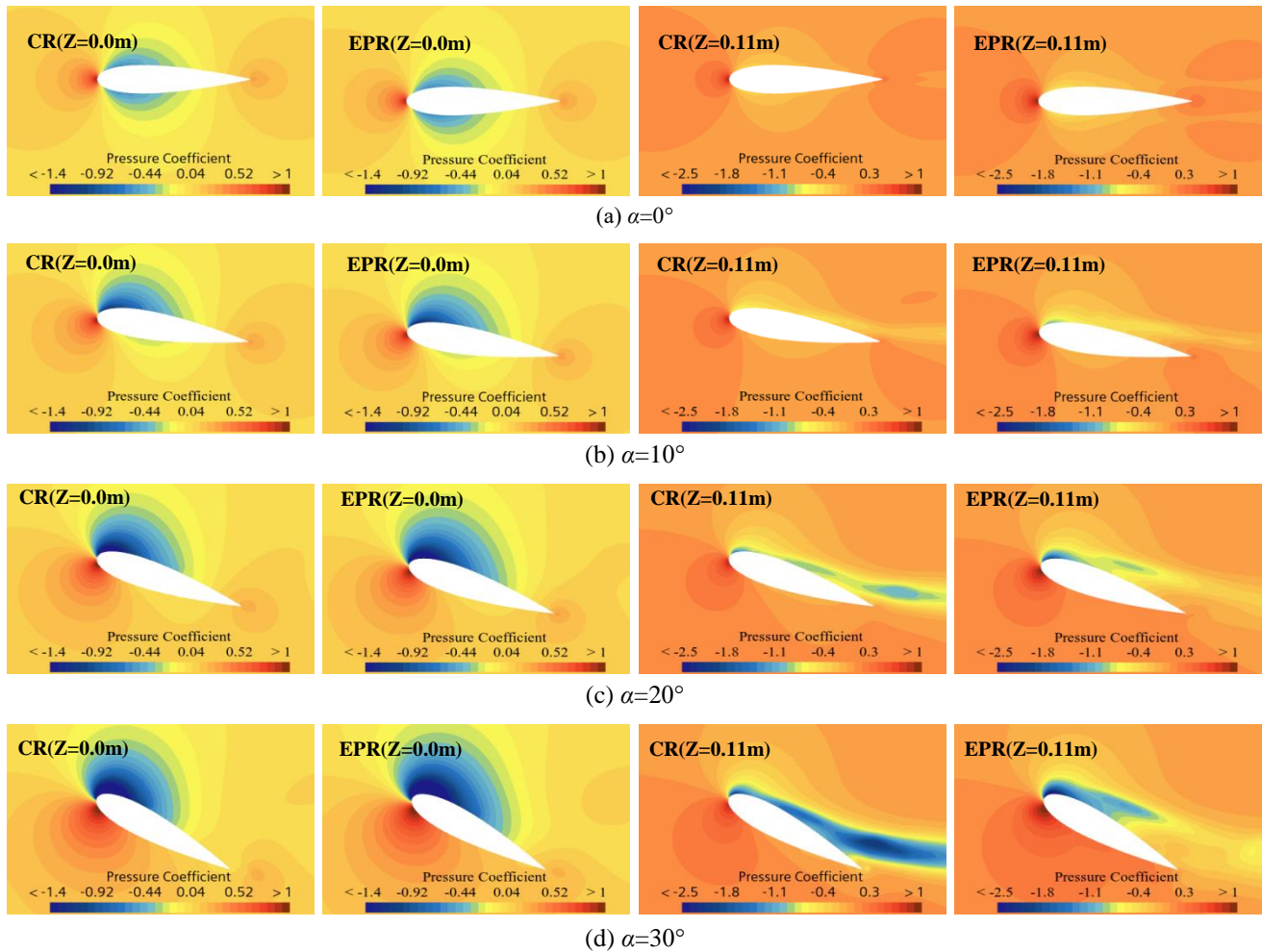


Fig. 15 Pressure distributions on horizontal cross-sections  $Z=0.0\text{m}$  and  $Z=0.11\text{m}$  at different rudder angles

## 7. Optimization design results

As analyzed in the preceding analysis, the end plate effectively suppresses transverse flow and improves rudder performance. To further optimize this effect, the end plate configuration must be determined to achieve optimal rectification of the end flow around rudder blade. In this work, a rectangle end plate is used, with a thickness of  $0.005C$  and rounded corner having a radius of  $0.05C$ . The impacts of the chordwise length before leading edge ( $c$ ), the chordwise length after trailing edge ( $d$ ), and the half width ( $b$ ) on the efficacy of the end plate are investigated. The goal is to determine the optimal values of these parameters through numerical simulations.

### 7.1 Width of end plate

Firstly, the half width ( $b$ ) of the end plate is examined. Numerical simulations are conducted to evaluate the hydrodynamic performances of EPR with varying end plate widths, while keeping  $c=d=0.05C$ . The values for half width span from  $0.13C$  to  $0.18C$ , as shown in Table 1. To comprehensively assess the effect of end plate width under different hydrodynamic load conditions, simulations are performed at rudder angles of  $0^\circ$ ,  $10^\circ$ ,  $20^\circ$ ,  $30^\circ$  and  $40^\circ$ . Fig. 16 presents the calculated hydrodynamic forces for EPRs at different rudder angles. Since rudders generate no lift at  $\alpha=0^\circ$ , the corresponding results are not displayed. As shown in the figures, the lift, drag, and lift-to-drag ratio all increase with greater end plate width. However, the trends in hydrodynamic forces, especially drag, show distinct variations at different rudder angles with these differences primarily reflected in the rates of increase.

Concerning the lift, the results at different rudder angles increase remarkably with the widening of the end plate, and the increment becomes more substantial as the rudder angle increases. For rudder angles of  $10^\circ$

and 30°, the lift exhibits a slight linear trend, whereas the increase rates of the lift values at 20° and 40° gradually decline as the end plate width increases when the  $b/C$  is smaller than 0.16. Regarding the beneficial force for a ship rudder, the lift is expected to be maximized. As a result, when considering the lift alone, a wider end plate is preferable. EPR drags follow a similar trend to the corresponding lifts, increasing with the end plate width. However, the trends of variation in drag with respect to the end plate width at 20° and 30° exhibit a significant nonlinearity. Although both lift and drag increase as the end plate width increases, it is smaller in the drag than in the lift, and this disparity becomes more pronounced at larger end plate widths. Therefore, the lift-to-drag ratio increases gradually with the widening of the end plate. This ratio increase at 10° and 30° is particularly notable when the ratio  $b/C$  is smaller than 0.16.

Furthermore, EPR drags with end plates of different widths under no steering conditions are displayed in Fig. 17. The drag increases gradually with the end plate width and has a sharp increase when  $b > 0.16C$ . Moreover, the end plates are detrimental to the drag performance of the rudder when the ship is in straight sailing mode.

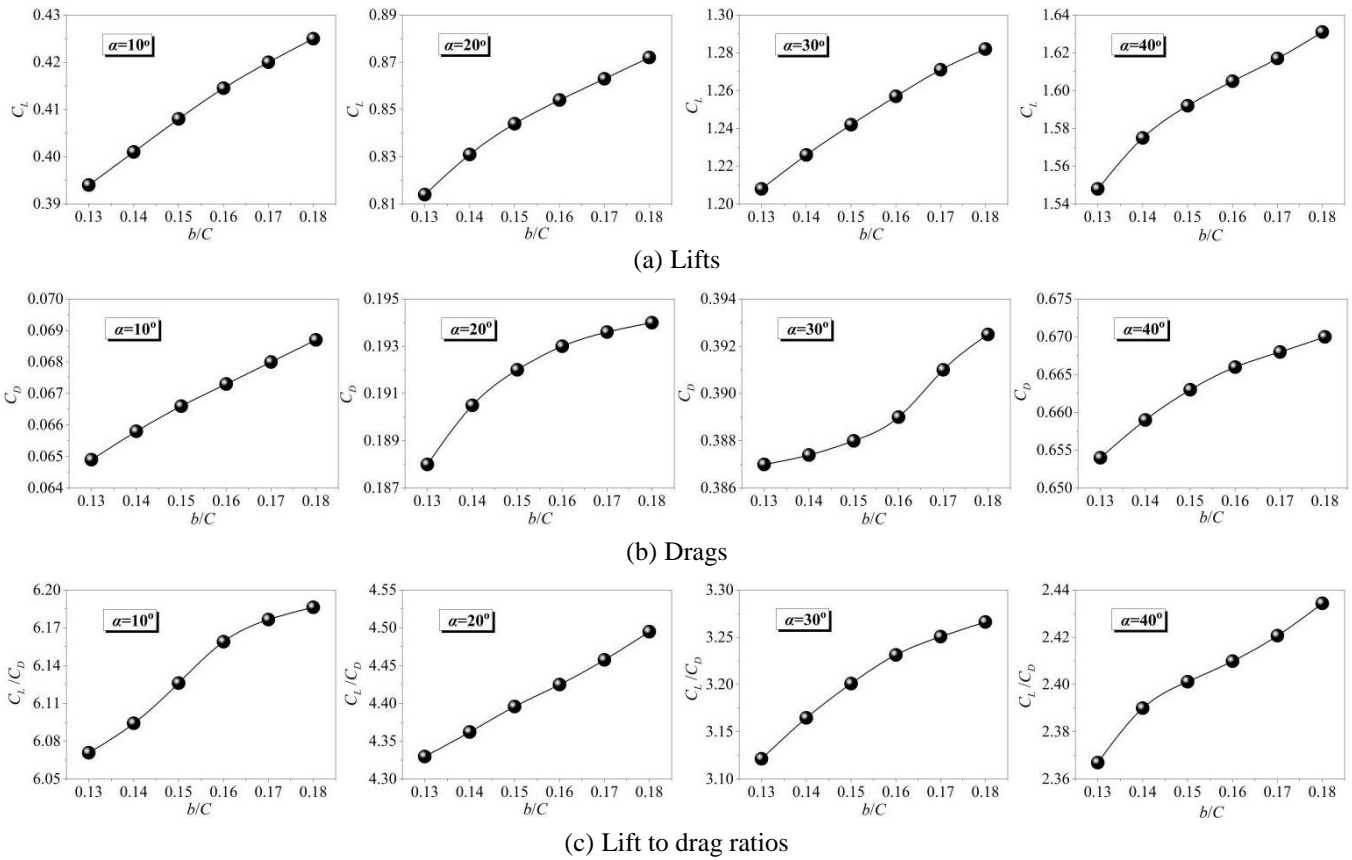


Fig. 16 Hydrodynamic forces of EPRs with various wide end plates at different rudder angles

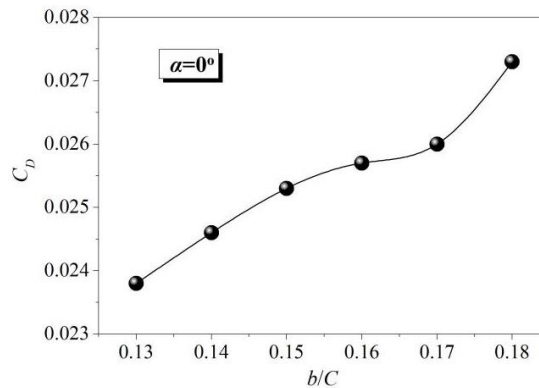
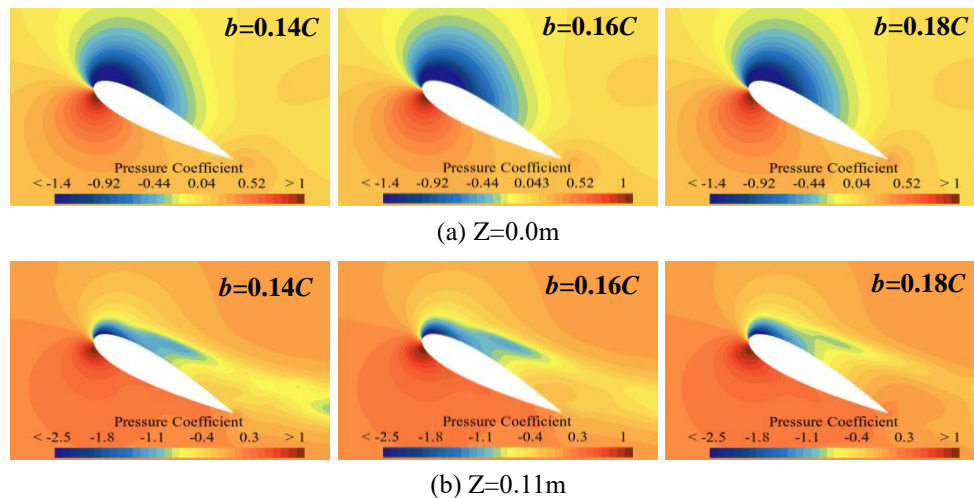


Fig. 17 Drags of EPRs with various wide end plates under no steering condition

To reveal the effect of the end plate of different widths on the pressure distribution around the rudder blade, pressure distributions on horizontal cross-sections  $Z=0.0$  m and  $0.11$  m for  $b=0.14C$ ,  $0.16C$ , and  $0.18C$  at  $\alpha=30^\circ$  are illustrated in Fig. 18. The end plate's width has an impact on the pressure distribution around the rudder blade, especially for the pressure near the end plates. It is clear that the impact of end plate's width on the pressure distributions near lower and upper surfaces on the cross-section  $Z=0.0$  m can be neglected. However, the end plate's width has an evident impact on the pressure distribution near the ends of rudder blade, referring to the results on the cross-section  $Z=0.11$  m displayed in Fig. 18(b). As the end plate width increases, the high-pressure region on the lower surface of the rudder blade extends noticeably rearward toward the trailing edge and bypasses the trailing edge to spread onto the upper surface. This results in the gradual formation of a local high-pressure region near the trailing edge. Simultaneously, the local stagnation point on the upper surface shifts toward the leading edge. Additionally, the pressure on the upper surface at the rudder blade's ends increases from the section shoulder to the trailing edge with the widening of the end plate. However, both the high- and low-pressure core expand to a certain extent, and this phenomenon is more pronounced for the high-pressure core.

Consider that lift is generated by the pressure difference between the upper and lower surfaces of the rudder section, the increase in pressure on the upper surface near the trailing edge vicinity is offset by the growth in pressure on the lower surface at the trailing edge vicinity near the rudder blade's ends; moreover, the lift increases with the end plate's width. Furthermore, the drag mainly originates from the pressure difference between the front and back of the rudder section, where the increase in the pressure at the front is greater than that at the back. Thus, the drag increases with the end plate's width.

Overall, the results indicate that larger end plate width increases both lift and drag, yet the lift gain exceeds the drag gain under a certain rudder angle. Therefore, the rudder efficiency increases with larger end plate width. However, considering the drag performance under no steering conditions, the width of the end plate is set to be  $b=0.16C$  for optimization purposes.



**Fig. 18** Pressure distributions on horizontal cross-section  $Z=0.0$ m and  $Z=0.11$ m for  $b=0.14C$ ,  $0.16C$  and  $0.18C$  at  $\alpha=30^\circ$

## 7.2 Chordwise length before leading edge

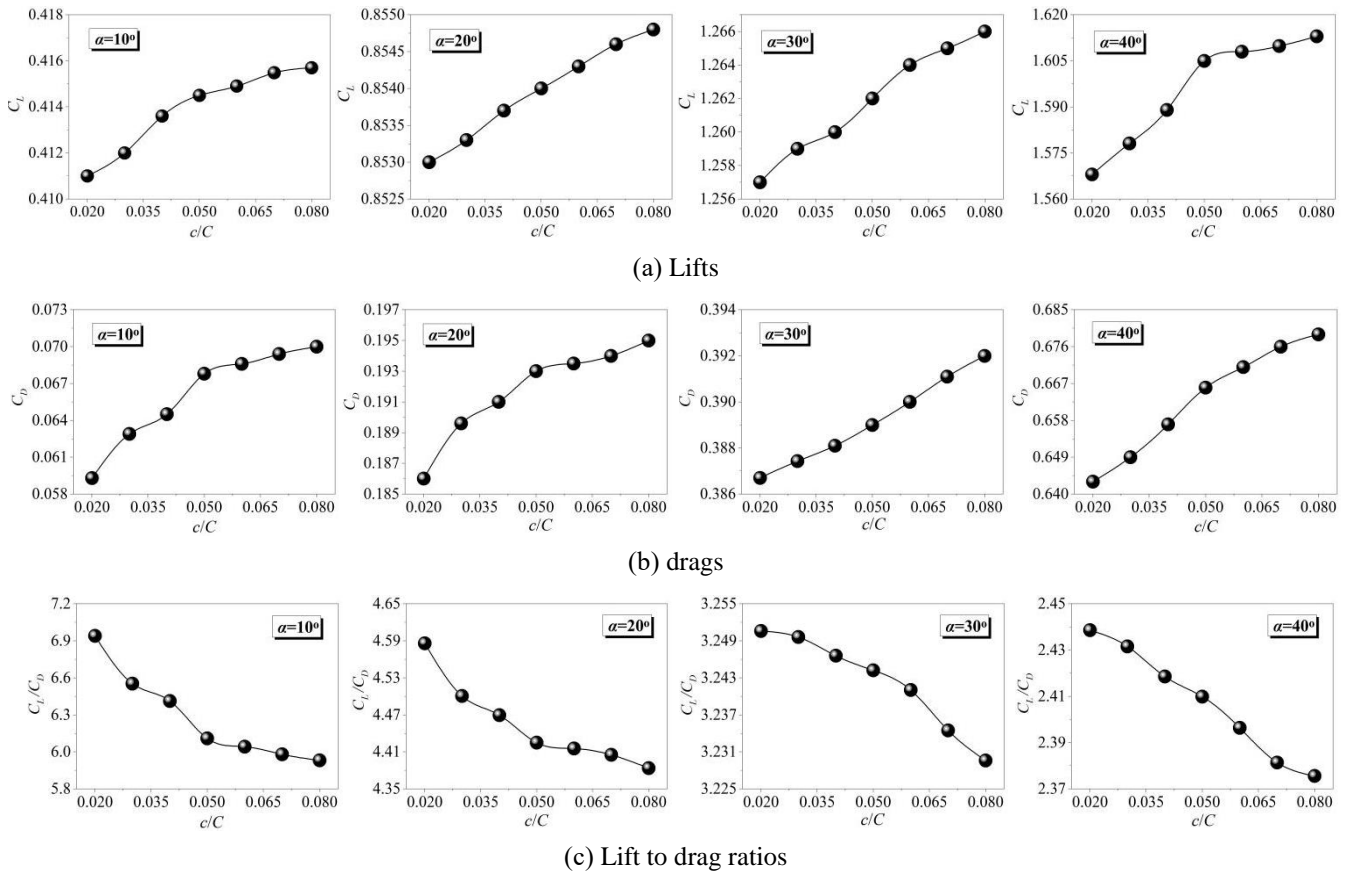
Building on the findings related to end plate width, this section further investigates the impact of the chordwise length before the leading edge ( $c$ ) on the rudder's hydrodynamic performance. This parameter is hereafter referred to as Chordwise Length Before the leading edge (CLB), and the goal is to determine its optimal value. Therefore, the hydrodynamic performances of EPR with end plates of different CLBs ( $b=0.16C$ ,  $d=0.05C$ ) are simulated, where the CLBs span from  $0.02C$  to  $0.08C$ , as given in Table 1.

Fig. 19 displays the lifts, drags, and the corresponding lift-to-drag ratios of EPR at four rudder angles ( $10^\circ$ ,  $20^\circ$ ,  $30^\circ$  and  $40^\circ$ ). Both the lifts and drags show an increasing trend with the CLB at different rudder angles. Overall, the increase rates of the hydrodynamic forces drop considerably when CLB is greater than

0.05C. However, the lift-to-drag ratios show a decreasing trend due to the magnitude of the drag associated with CLB exceeds when the lift increased. Therefore, the increase of CLB can improve the rudder effectiveness, while it also reduces the rudder efficiency in a certain dimension. Further analysis of Fig. 19 reveals that, even though the CLB has an impact on the rudder’s hydrodynamic forces, its influence on the rudder’s lift is very weak. The maximum lift for the case with  $c=0.08C$  shows only a 2.8% increase compared to the minimum lift observed for  $c=0.02C$  across different rudder angles. However, the impact of CLB on the rudder’s drag is more pronounced, with a maximum difference of 18.2% between the cases. Therefore, the lift-to-drag ratio decreases when CLB increases.

Added to that, EPR drags with end plates of different CLBs under no steering conditions are displayed in Fig. 20. It is clear that the drag increases gradually with CLB and its variation is linear when CLB is greater than 0.05C, yielding a relatively gentle increase trend when  $c \leq 0.04C$ .

Based on the above analysis, it is clear that as CLB increases, the rudder’s efficiency shows a slight increase, coupled with the decline of efficiency as the rudder angle increases as well as the rise of drag under no steering conditions. Thus, a smaller CLB is required, and it is set to  $c=0.03C$  for the rudder considered in this work.



**Fig. 19** Hydrodynamic forces of EPR with end plates of different chordwise lengths before leading edge at various rudder angles

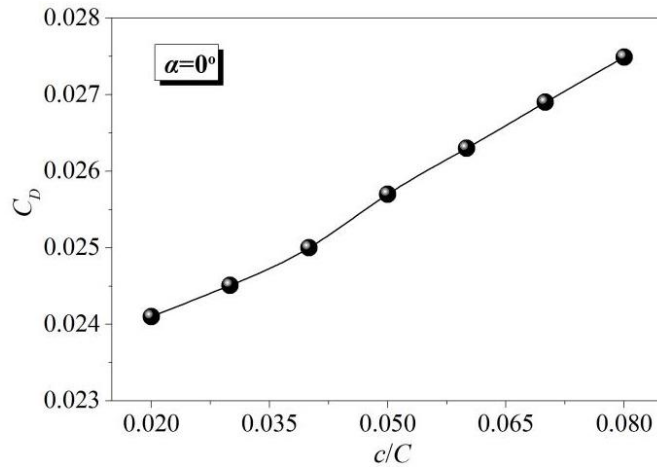


Fig. 20 Drags of EPR with end plates of different chordwise lengths before leading edge under no steering condition

### 7.3 Chordwise length after trailing edge

Finally, the impact of the end plate’s chordwise length after the leading edge ( $d$ ) on the rudder’s hydrodynamic performance is analyzed and the end plate’s optimal Chordwise Length After the leading edge (CLA) is determined based on above findings. EPR hydrodynamic performances with end plates of varying CLAs ( $b=0.16C, c=0.03C$ ) are simulated. The CLAs span from  $0.02C$  to  $0.08C$ , as indicated in Table 1.

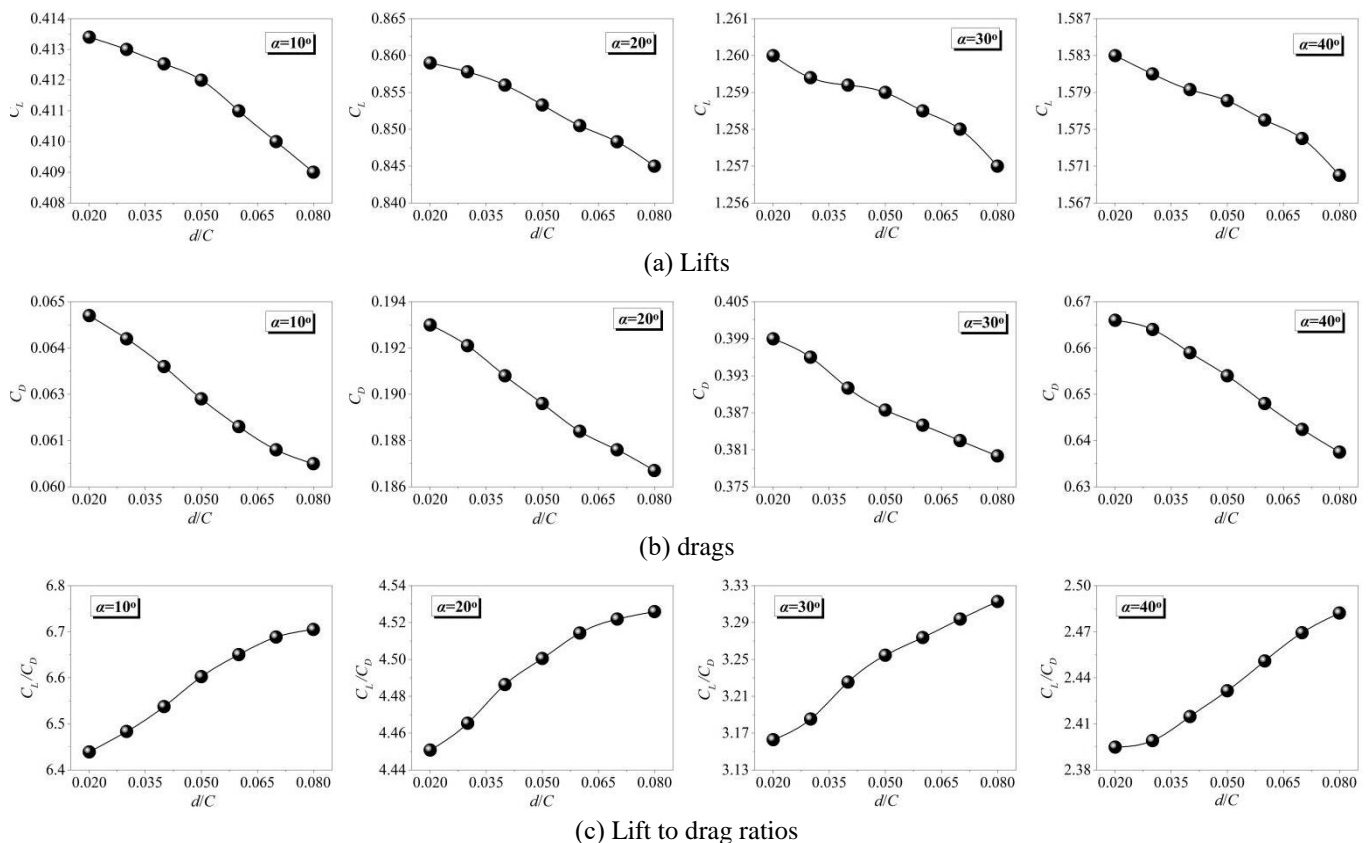
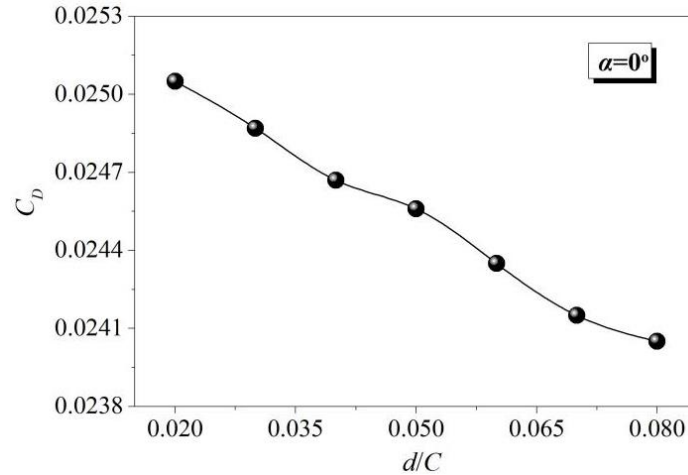


Fig. 21 Hydrodynamic forces of EPR with end plates of different chordwise lengths after leading edge at various rudder angles

Fig. 21 displays EPR simulated hydrodynamic forces with end plates under different CLAs. It can be seen that the impact of CLA on the rudder’s hydrodynamic forces exhibits a full opposite trend compared to CLB. Both lift and drag of EPR show a decreasing trend with the CLA increasing at different rudder angles. While the lift-to-drag ratios show an increasing trend. This is mainly due to the magnitude of the drag’s decrease associated with CLA that exceeds the lift’s decrease. Therefore, the increase of the end plate’s CLA

is detrimental to the rudder effectiveness and improves the rudder efficiency to some extent. Moreover, Fig. 22 displays EPR drags with end plates of different CLAs under no steering conditions. The drag decreases gradually with the increase of CLA.

Overall, considering that the rate of lift's decrease increases significantly and the efficiency rate increase is moderately reduced when CLA exceeds  $0.05C$ , the optimal CLA is set as  $d=0.05C$ . Table 4 presents the final optimal geometric parameters of end plates and their corresponding hydrodynamic forces.



**Fig. 22** Drags of EPRs with end plates of different chordwise lengths after leading edge under no steering condition

**Table 4** Optimal geometric parameters and corresponding hydrodynamic forces

$\alpha$	$b$	$c$	$d$	$C_L$	$C_D$	$C_L/C_D$
$0^\circ$	$0.16C$	$0.03C$	$0.05C$	----	0.024	----
$10^\circ$				0.412	0.062	6.60
$20^\circ$				0.853	0.190	4.50
$30^\circ$				1.259	0.387	3.25

## 8. Conclusions

The impact of end plates on the hydrodynamic performance of rudder blade is investigated, and their configuration is determined for optimal flow rectification. A NACA0020 profile ship rudder is studied in detail, and the DES method is employed for numerical simulations. The following conclusions can be drawn:

1. The optimal grid partitioning strategy is determined through grid independence analysis, and the method used in this study is assessed based on the corresponding experimental results. The pressure distribution on the conventional rudder surface reveals that the endwise transverse flow reduces the rudder efficiency to some extent;

2. The end plates can effectively improve the rudder's effectiveness and efficiency through suppressing the transverse flow around the rudder blade and inhibiting the turbulent flow on the upper surface of the rudder blade. Moreover, the end plates can obviously delay the rudder stall phenomenon. The configuration of the end plate is determined for optimal rectification for end flow of rudder blade from effectiveness and efficiency. The end plate's optimal width, chordwise length before leading edge, and chordwise length after trailing edge are 0.16, 0.03 and 0.05 times the chord length of rudder blade for the rudder studied in this work, respectively.

This work provides technical guidance for the design work of rudder with end plates, helping to improve the maneuverability and energy efficiency of ships. However, the research conclusions are subject to the specific rudder configuration and inflow condition, and their applicability needs further investigation. Moreover, this study is primarily confined to open water conditions without accounting propeller and hull

effects. As a result, subsequent work will incorporate hull and propeller influences to conduct further research on the performance and optimization of EPR, thereby refining the conclusions drawn in this work.

## Acknowledgments

This research is financially supported by the Liaoning Provincial Natural Science Foundation of China (Grant No. LJKMZ20220367) and the Fundamental Research Funds for the Central Universities (3132023121).

## REFERENCES

- [1] Kim, J.H., Choi, J.E., Choi, B.J., and Chung, S.H., 2014 Twisted rudder for reducing fuel-oil consumption. *International Journal of Naval Architecture and Ocean Engineering*, 6(3), 715-722. <https://doi.org/10.2478/IJNAOE-2013-0207>
- [2] Omweri, O.E., Shen, H., Su, Y., 2021. Study on the design procedure of rudder attached thrust fin for merchant ship based on computational fluid dynamics. *Ocean Engineering*, 234(6), 109263. <https://doi.org/10.1016/j.oceaneng.2021.109263>
- [3] Kerwin, J.E., Mandel, P., Lewis, S.D., 1972. An experimental study of a series of flapped rudder. *Journal of Ship Research*, 16(4), 225-234. <https://doi.org/10.5957/jsr.1972.16.4.221>
- [4] Olson, C.R., 1955. Effects of various linkage ratios on the free-stream hydrodynamic characteristics of an all-movable flapped rudder. Washington DC: David Taylor Model Basin.
- [5] Hou, L.X., Yang, J., Hu, A.K., Chang, X., Lin, Y., Yin, L.L., Chuang, Z.J., 2022. Hydrodynamic characteristic investigations of a collaborative spoiled rudder under open water conditions. *Ocean Engineering*, 253, 111251. <https://doi.org/10.1016/j.oceaneng.2022.111251>
- [6] Hou, L.X., Lin, Y., Zhu, J.Q., Wang, Q.C., Yang, J., Liang, H.F., Chang, X., 2023. Two-dimensional study on the hydrodynamic performance of collaborative spoiled rudder. *Ocean Engineering*, 271, 113826. <https://doi.org/10.1016/j.oceaneng.2023.113826>
- [7] Sasaki, N., Kuribayashi, S., Fukazawa, M., Atlar, M., 2020. Towards a realistic estimation of the powering performance of a ship with a gate rudder system. *Journal of Marine Science and Engineering*, 8(1), 43. <https://doi.org/10.3390/jmse8010043>
- [8] Carchen, A., Turkmen, S., Piaggio, B., Shi, W., Carchen, A., 2020. Investigation of the manoeuvrability characteristics of a Gate Rudder system using numerical, experimental, and full-scale techniques. *Applied Ocean Research*, 106, 102419. <https://doi.org/10.1016/j.apor.2020.102419>
- [9] Abramowicz-Gerigk, T., Burciu, Z., Jachowski, J., Kreft, O., Majewski, D., Stachurska, B., Sulisz, W., Szymkiewicz, P., 2021. Experimental method for the measurements and numerical investigations of force generated on the rotating cylinder under water flow. *Sensors*, 21(6), 2216. <https://doi.org/10.3390/s21062216>
- [10] Abramowicz-Gerigk, T., Burciu, Z., 2022. Investigations of hydrodynamic force generated on the rotating cylinder implemented as a bow rudder on a large-scale ship model. *Sensors*, 22, 9137. <https://doi.org/10.3390/s22239137>
- [11] Li, F., Hu, H.B., Li, B.H., Jiang, S.H. 2020. Current development and technology status of high performance rudders. *Chinese Journal of Ship Research*, 5(3), 61-74.
- [12] Ou, L.J., Ma, Z.C., 2017. Analysis on hydrodynamic performances of swash plate rudder and application in ship. *Guangdong Shipbuilding*, 155, 30-33.
- [13] Zaky, M., Sano, M., Yasukawa, H., 2018. Improvement of maneuverability in a VLCC by a high lift rudder. *Ocean Engineering*, 165, 438-449. <https://doi.org/10.1016/j.oceaneng.2018.07.030>
- [14] Liu, L., Zhang, B.J., Zhang, H., Gong, J.Y., Tian, Z., Guo, S.H., Bao, Y.B., Zheng, X., 2024. Study on numerical simulation and mitigation of parametric rolling in a container ship under head waves. *Brodogradnja*, 75(3), 75305. <https://doi.org/10.21278/brod75305>
- [15] Lee, S.H., Paik, K.J., Hwang, H.S., Eom, M.J., Kim, S.H., 2021. A study on ship performance in waves using a rans solver, part 1: comparison of power prediction methods in regular waves. *Ocean Engineering*, 227(86), 108900. <https://doi.org/10.1016/j.oceaneng.2021.108900>
- [16] Hou, L.X., Wang, Q.C., 2022. Investigation about the hydrodynamic coupling characteristics of contra-rotating azimuth propulsor. *Brodogradnja*, 73(4), 79-105. <https://doi.org/10.21278/brod73405>
- [17] Yurtseven, A., Aktay, K., 2023. The numerical investigation of spindle torque for a controllable pitch propeller in feathering maneuver. *Brodogradnja*, 74(2), 95-108. <https://doi.org/10.21278/brod74205>
- [18] Tian, M.J., 2015. Research on the design and the hydrodynamic performance of the ship flap rudder. College of Aerospace Engineering, Nanjing University of Aeronautics and Astronautics.
- [19] Liu, J.L., Quadvlieg, F., Hekkenberg, R., 2016. Impacts of the rudder profile on manoeuvring performance of ships. *Ocean Engineering*, 124, 226-240. <https://doi.org/10.1016/j.oceaneng.2016.07.064>

- [20] Shin, Y.J., Kim, M.C., Lee, J.H., Song, M.S., 2019. A numerical and experimental study on the performance of a twisted rudder with wavy configuration. *International Journal of Naval Architecture and Ocean Engineering*, 11, 131-142. <https://doi.org/10.1016/j.ijnaoe.2018.02.014>
- [21] Yang, Y., Wang, Z.L., Geng, J.M., 2020. Numerical Study on the flap rudder hydrodynamic simulation based on CFD. *Ship Science and Technology*, 42(4), 46-50.
- [22] Sukas, O.F., Kinaci, O.K., Bal, S., 2021. Asymmetric ship maneuvering due to twisted rudder using system-based and direct CFD approaches. *Applied Ocean Research*, 108, 102529. <https://doi.org/10.1016/j.apor.2021.102529>
- [23] Park, I., Paik, B., Ahn, J., Kim, J., 2021. The prediction of the performance of a twisted rudder. *Applied Sciences*, 11(15), 7098. <https://doi.org/10.3390/app11157098>
- [24] Tong, X.D., Chen, H.Y., Dong, X.Q., Chen, Y., 2021. Experimental and numerical investigations on the unsteady thrust of a propeller in presence of an upstream rudder. *Ocean Engineering*, 237(4), 109644. <https://doi.org/10.1016/j.oceaneng.2021.109644>
- [25] Zhang, W., Ning, X., Li, F., Guo, H., Sun, S., 2021. Vibrations of simplified rudder induced by propeller wake. *Physics of Fluids*, 33(8), 083618. <https://doi.org/10.1063/5.0058968>
- [26] Shur, M.L., Spalart, P.R., Strelets, M.K., Travin, A.K., 2008. A hybrid RANS-LES approach with delayed-DES and wall-modelled LES capabilities. *International Journal of Heat and Fluid Flow*, 29 (6), 1638-1649. <https://doi.org/10.1016/j.ijheatfluidflow.2008.07.001>
- [27] Feng, C.Q. 1989. Ship flap rudders. National Defense Industry Press.